J Infrared Milli Terahz Waves (2011) 32:434–450
DOI 10.1007/s10762-011-9767-8

Active Sparse-Aperture Millimeter-Wave Imaging Using Digital Correlators

Wilson Caba · Glenn Boreman

Received: 18 September 2010 / Accepted: 20 January 2011 /
Published online: 5 February 2011

Abstract Millimeter-wave imaging systems have desirable characteristics, particularly in their ability to form images of objects obscured by various barrier materials. However, the relatively long wavelength of the millimeter-band implies a penalty in angular resolution, usually compensated using large-aperture systems. Synthesized apertures provide the desired collecting area with a reduced number of discrete detectors. In this research we designed, built, and characterized the performance of a prototype sparse-aperture imaging system, utilizing an active 94 GHz source. Discrete sensors were used to sample the radiation field backscattered from the object. The signals were down-converted using heterodyne receivers with digital in-phase and quadrature detection. Signal correlations were performed using the digitized data sets to reconstruct millimeter-wave images. Image-quality performance was experimentally evaluated using four different non-redundant aperture configurations, with good agreement to the theoretical expressions. The feasibility of digital electronic-focusing correction was also demonstrated over an object range from 400 to 700 mm.

Keywords Active millimeter-wave imaging · Aperture synthesis · Digital correlation · Digital phase detection

1 Introduction

Millimeter waves (mmW) have been used to image through elements opaque in the visible and infrared. Systems capable of generating imagery of buried landmines and unexploded ordnances [1], concealed weapons [2], and inspection of civil structures [3] have been reported in the literature. This ability to image in a noninvasive way can be used to image objects concealed with clothing or behind barriers. With the low atmospheric absorption

W. Caba (✉) · G. Boreman
CREOL – College of Optics and Photonics, University of Central Florida, 4000 Central Florida Blvd., Orlando FL 32816, USA
e-mail: wcaba@knights.ucf.edu

G. Boreman
e-mail: boreman@creol.ucf.edu

experienced by radiation at 94 GHz [4], large standoff distances could potentially be achieved.

Millimeter-wave imagers, as a result of their inherently low angular resolution, need to have relatively large collecting apertures, compared to visible and infrared systems. The challenges brought by an enlarged aperture can be minimized by using aperture synthesis techniques. Based on approaches used in radio astronomy, an array of coherent detectors can be used to synthesize a large aperture using smaller detectors. Sampling the electric fields across the pupil plane can be used to reconstruct the spatial Fourier spectrum of an intensity distribution, and an image can be generated using Fourier inversion. The principle of image reconstruction is based on the Fourier transform relationship between the visibility function and the intensity distribution. A pair of detectors separated a distance D, called the baseline, determines a single value of the visibility function at a spatial frequency corresponding to the inverse of the baseline distance. As a consequence, the resolution of such a system depends on the maximum baseline, and the number of different baselines used, which in turn determine how the visibility function is sampled [5].

To sample the maximum amount of spatial frequency points, an array must have a correlator for every pair of detectors. The amount of detector pairs of an array grows with the square of the number of detectors [6]. This is both an advantage and a disadvantage. The advantage lies in a significant increase of the sampled points of the visibility function, but also implies a growth in the number of correlators needed, thus impacting the degree of miniaturization achievable in the synthesized aperture. A number of approaches have been used to generate imagery using interferometric techniques, which have been successful. They however suffer some limitations inherent in the context of the passive-system configuration. The spatial incoherence of passive sources requires that all detectors are measured at the same time. This impossibility of time multiplexing means that virtual arrays cannot be created by displacing the detectors in a single scan. A system with detectors located in a circular array is described in [7] and a one-dimensional array with minimum redundancy is described in [8]. A coherent-illumination active imaging system can take advantage of time-multiplexed scans, as described in [9]. However, this system requires the target to be displaced in two dimensions to obtain the images. Interferometric near-field millimeter-wave imaging have also been reported in the literature, but these approaches lack either flexibility in detector configuration [10] or require the use of sweeping wideband radiation and more complicated signal processing [11]. A flexible array is desirable for the study of the effects of different configurations, as well as their effect in overall image quality. Wideband imaging provides several advantages, such as high depth of field and elimination of speckle, but comes at the expense of more complicated transceivers and significantly more complicated signal processing.

In our study, a configurable array of coherent detectors was used to scan quasi-monochromatic backscattered radiation from targets located within the cone of the radiation pattern of an antenna serving as an illuminating source. The active system used in this study is capable of creating a virtual array of detectors by displacing the detectors instead of the targets. Having the ability of rearranging the receiving array allows direct measurement and comparison of commonly used configurations. Every point in the visibility function is obtained by correlation of the complex signals measured by the detectors. Therefore, the accuracy of the reconstruction is dependent on the phase-detection scheme. For the test bed used and described in this research, we used an approach that combines an analog heterodyne down-conversion stage and a digital quadrature demodulation stage. We chose down-conversion to radio frequencies (RF) over up-conversion to optical frequencies because the former method offers more flexibility in component availability, ease of wave

guiding, and better cost effectiveness. Phase detection is then performed offline after the RF signals have been sampled and stored. Offline phase detection is what gives our system its digital-focusing capability.

Because blackbody radiation of objects at room temperature is so low in the mmW portion of the spectrum (about 8 orders of magnitude lower than IR), an active source is needed to obtain sufficient contrast for indoor imaging. We report on a reconfigurable, active, millimeter-wave imaging system using a synthesized antenna and digital correlators. A set of experiments measure the resolution an image quality for one-dimensional and two-dimensional arrays. A study on the effects of detector configuration on the point spread function is also included.

2 Test bed

The test bed seen in Fig. 1 was designed to achieve the following requirements: active illumination, subwavelength sensor-positioning accuracy, coherent detection, and automated operation. The frequency of operation is 94 GHz (λ=3.19 mm), generated using a Gunn oscillator. The output of the Gunn oscillator is then amplified to 24 dBm (~250 mW) and channeled to the center of the platform using WR-10 waveguide, which was used for all interconnections. A square horn antenna with 24° beamwidth directs the radiation in the forward direction. Two-dimensional scanning was achieved by mounting the detectors on six linear-actuator arms, mounted on a rotary stage, all controlled under LabVIEW. The longest radial extension of the arms, from the center of the test bed, was 450 mm, including 50 mm offset. The resolution of the linear actuator was about 950 steps per mm. The angular rotation was controlled using a rotary stage with a maximum resolution of 1,080,000 steps per revolution (about 6 μrad).

2.1 Digital phase detection

Coherent phase detection of millimeter waves was achieved using a technique developed for this system. Millimeter-wave signals were down-converted from 94 GHz to 20 MHz

Fig. 1 The test bed system with 6 linear translation arms mounted on a rotary stage. The illuminating source is at the center. Detectors, mounted on linear actuators, can extend a maximum of 450 mm. Components lie on a circular plate 55.9 cm in diameter

using a heterodyne analog down-conversion stage. In the offline processing section, a conventional quadrature demodulator, shown in Fig. 2, was enabled using digital equivalents for power dividers, mixers, phase shifters, and low pass filters. The substitution of analog components by digital equivalents minimizes the noise that is typically experienced by analog demodulators. Digital processing and calculations are performed using Matlab. The main reasons for use of digital equivalents of analog I/Q demodulators are the elimination of amplitude and phase mismatches, exact performance of filters, the ability to use zero-phase filters. This allowed the measurements to be performed well away from the dc component, reducing effects of $1/f$ noise.

The physical components of Fig. 2 were thus substituted by digital equivalents. The mixers were emulated by multiplying the arrays containing the sampled incoming and reference signals. A 90° phase-delayed version of the reference was obtained using the quadrature property of the Hilbert transform [12]. LPF_1 and LPF_2 can be simulated using any type of digital low-pass filter. For these experiments, we found that a second-order Butterworth filter with a cutoff frequency of 0.002 of the sampling frequency produces ripples of less than 1% of the maximum amplitude. Single values of I and Q are calculated by averaging the outputs of LPF_1 and LPF_2.

3 Experimental methods

The experiments were performed with the test bed lying horizontally on a table and the targets placed above the test bed. To adjust the distance between the targets and the test bed, the targets were mounted on a lift. Millimeter-wave foam absorbers (ECCOSORB CV) were placed behind the targets to minimize unwanted reflections.

3.1 Performance metric

To compare the point-source reconstruction performance of various configurations we used the peak-to-integrated-sidelobe-ratio (PISLR), which is a figure of merit equal to the logarithm of the ratio of the energy contained in the center lobe of the point spread function (PSF) and the energy in the sidelobes, given in decibels, which is given by Eq. (1).

$$PISLR = 10\log\left\{\frac{\int_0^{2\pi}\int_0^{FWHM} PSF_{array}(\rho,\varphi)\rho d\,\rho d\varphi}{\int_0^{2\pi}\int_{FWHM}^{\max} PSF_{array}(\rho,\varphi)\rho d\,\rho d\varphi}\right\} \tag{1}$$

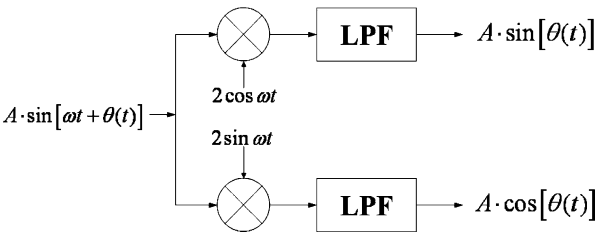

Fig. 2 Conventional quadrature demodulator model

3.2 Scan parameters for one-dimensional measurements

The first set of experiments was intended to measure the impulse response of the system in one dimension. A ball bearing 16 mm in diameter (5/8 inches), illuminated by the source, was the smallest suitable target that could be unambiguously distinguished at a distance between 300 and 900 mm, located immediately above the center of the test bed at a distance of 430 mm. The relatively large dimension of the point source was because reflections from smaller objects were closer to the noise level of the detection section, making the reconstructions less than acceptable. A 40-element array was simulated by displacing one detector by about 62 mm (19.5 wavelengths). The parameters used are shown in Table 1, and Fig. 3 shows a schematic of the measurement.

Figure 4 shows the calculated and measured values of the phase, at the plane of the detectors, as a function of the distance from the center. The discrepancy between the absolute values of the calculated and measured values can be disregarded, as only the relative phase difference is of interest. The difference between calculated and measured values is approximately 150°, with a standard deviation of 28°. This level of accuracy means that the measured data points are, on average, within 2/25 of a wavelength of the expected values.

3.3 Image-reconstruction process

Electronic, or numerical, focusing is one of the features made possible by our offline digital signal processing approach, which allows calculations that are not possible with real-time imaging. The ability to focus is critical for imaging objects that are not in the far field, since the usual image reconstruction procedure using Fourier inversion is limited to far-field objects. Far fields and near fields are defined in terms of the ratios of the diameter of the collecting aperture D and the wavelength of the radiation. In a given system, the distance S that is considered to be in the far field is given by $S=D^2/4\lambda$ [13]. For our system, with a maximum collecting aperture of 900 mm, and wavelength of radiation $\lambda=3$ mm, the far field is approximately 67 m, which required digital-focusing procedures for the objects of interest. If the source coordinates are known, then a phase correcting term can be added to the spherical wavefront so it becomes a plane wave. Common algorithms for image reconstruction can now be used. This simulated lens, or phase correcting element, can be represented by multiplying each point in the pupil plane by a complex exponential. Using this approach, focus on any point in space can be obtained.

3.4 One-dimensional reconstruction results

The reconstructions of the measured point source are shown in Fig. 5a and b. Figure 5a is the reconstructed point source after using the digital focus algorithm and Fig. 5b is the

Table 1 Digitizer parameters for reconstruction experiments

Parameter	Value	Units
Sampling rate	200×10^6	Samples per second
Number of samples	32768	
Vertical range	200	mV_{pp}
Input Impedance	50	Ω

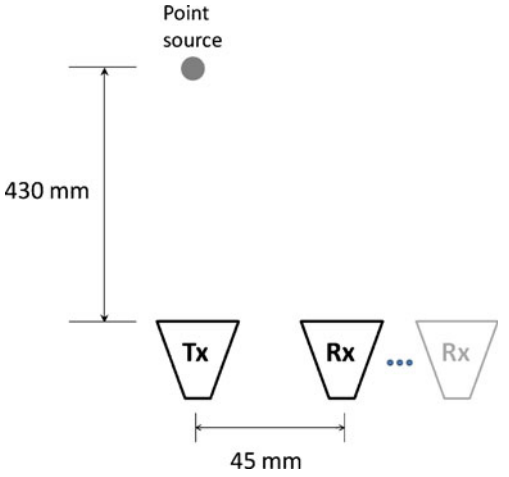

Fig. 3 Schematic for the experimental setup

reconstruction without using the focusing algorithm. On both plots the x-axis is the sine of the angular location of the source, with respect to the assigned reference, and the y-axis is the intensity. As a consequence of the use of the focusing algorithm, Fig. 5a appears centered in the plot. The plot was smoothed by performing an autocorrelation of the signals and by adding a pad of 100 zeros at each end of the array. The FWHM of the measured and calculated values is 2.4° and the PISLRs are 4.52 dB and 1.6 dB, for the calculated and measured values, respectively.

Figure 5b shows the reconstructed point source without applying the focusing algorithm. Under these circumstances, the location of the object is shifted and the angular location is given with respect to a different reference. The angular reference for Fig. 5b is taken with respect to the center of the simulated array. The calculated and measured values of the angular location of the point source are -9.63° and -10.36°, respectively. The relatively large dimension of the simulated array, 62.2 mm, compared to the point source location, 430 mm, means that the effects of near-field reconstruction are going to be noticeable. Without focusing, the FWHMs are 2.67° and 3.4°; whereas the PISLRs are 0.61 dB and -0.13 dB, for calculated and measured reconstructions, in that order. Also relevant is the loss in peak intensity for the unfocused reconstruction: it is only 66% and 61% of the focused intensity, for the calculated and measured values, correspondingly.

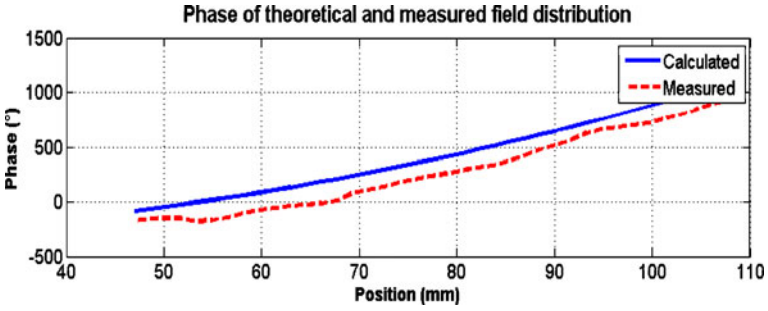

Fig. 4 Phase of theoretical and measured field distributions generated by a point source located 430 mm from the test bed

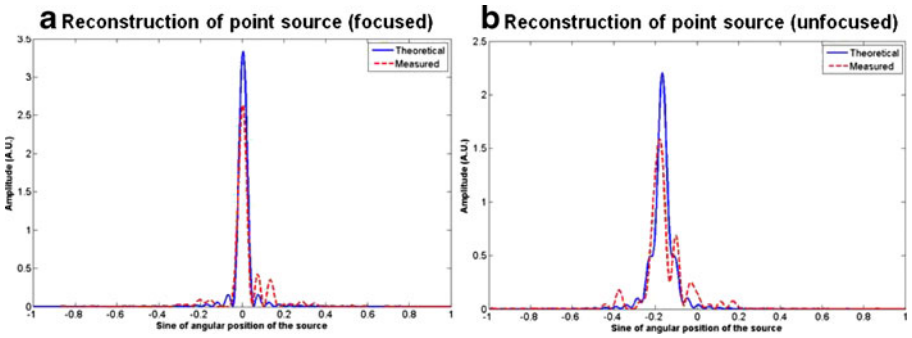

Fig. 5 Reconstruction of point source, **a** using digital focusing, **b** without using digital focusing

The following set of experiments is intended to apply the above-mentioned techniques to extended targets, namely a metallic ring. Figure 6 is a picture of the target sitting on a foam absorber. The dimensions of this target are 126 mm, for the outer diameter, and 84 mm for the inner diameter. The distance from the test bed to the target is 660 mm and the digitizer parameters are as specified in Table 1. Two sets of 40 data points were taken, with the distance between each data point being 1.6 mm (1/2 λ) and the separation between each set of 40 points being 105 mm.

The reconstruction process was similar to the one used for the point source measurements. Figure 7 shows the one-dimensional slices obtained for arrays along the x-axis ($\varphi = 0°$) and y-axis ($\varphi = 90°$). The similar results seen in both plots of Fig. 7 are a consequence of the symmetry of the target. The angular width of each peak agrees with what is expected to be measured for an object of the given dimensions: each peak ranges between 1.92° and 2.12°, measured at the FWHM point, and the measured diameter of the target is between

Fig. 6 Metallic ring used for the extended target reconstructions. Outer diameter: 126 mm, inner diameter: 84 mm. The one-dimensional sampling pattern consisted of two data sets of 40 points each. The separation between every point was ~1.6 mm (1/2 wavelength) and the separation between each data set was 105 mm. The data sets were separated from each other because of mechanical limitations imposed by the test bed design

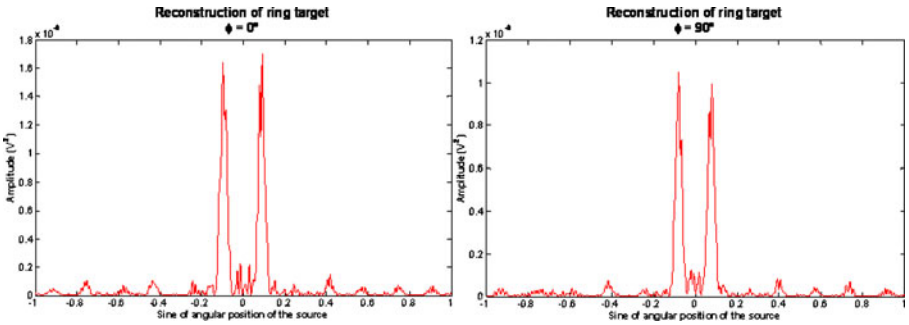

Fig. 7 Orthogonal one-dimensional reconstructions of ring target

10.8° and 12.6°. The angular dimensions for the target shown in Fig. 6, at 660 mm, are 1.81°, for the ring width, and 10.9°, for the full diameter.

3.5 Two-dimensional reconstructions

Two-dimensional reconstructions were obtained using the metallic ring shown in Fig. 6 as the object, at a distance of 660 mm from the test bed. In this set of experiments, a series of one-dimensional scans were performed at different angles and combined into a single two-dimensional array. The following figures show the distributions used to map the aperture-plane phase on the left, and the two-dimensional reconstructions on the right.

Figure 8 shows the target reconstruction when using a four-arm configuration. Each arm represents the phase of 40 sampled points with a spacing of 1/2 λ. The plot on the right is the reconstruction, which shows strong ringing as a consequence of the very low sampling density. Constructive and destructive interference is clearly visible, especially at the intersection of the orthogonal large intensity lines. Detection is possible, but the shape cannot be identified using this configuration. The separation between each group of 40 points, sampled in the same dimension, is 105 mm. This separation is consistent throughout all measurments. Total time to sample and generate the image was approximately 2 min.

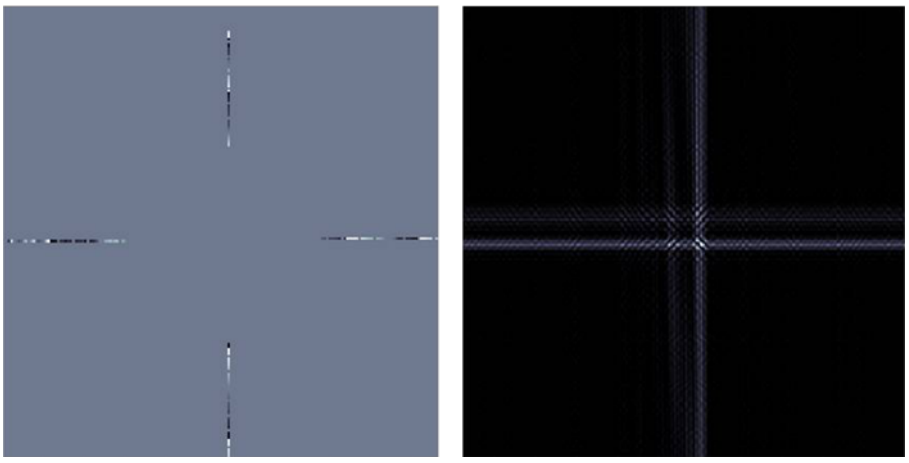

Fig. 8 Phase plot in the pupil plane (*left*) and reconstruction (*right*) of metallic ring using a 4-arm configuration

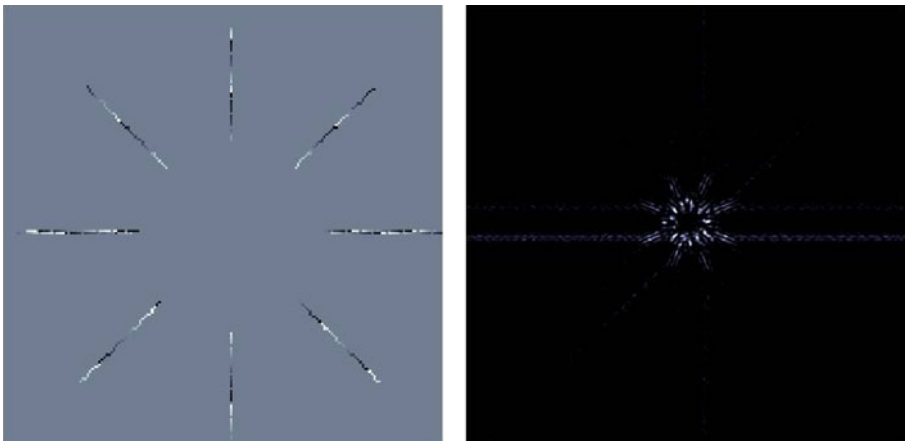

Fig. 9 Phase plot in the pupil plane (left) and reconstruction (right) of metallic ring using an 8-arm configuration

The use of eight arms with an angular separation of 45° generates a phase plot and a reconstruction as shown in Fig. 9. Separation between consecutive points is 1/2 λ, with 40 points per arm and a maximum span of 236 mm. This sampling configuration still presents strong ringing, but the object can be clearly identified as being circular. The resolution is as expected for the given diameter, about 2°, but ringing is still very strong. Sampling and reconstruction time for this scan was approximately 4 min.

Figures 10 and 11 are reconstructions obtained using 12- and 24-arm configurations, respectively. These reconstructions show a decrease in ringing as the number of sampled points increase. For the 24-arm configuration, a second parameter was adjusted, namely the spacing between consecutive points, which was increased from 1/2 λ to 1 λ. Increasing the sampling space decreased the collection time to 6 min, from a projected 8 min, without any noticeable decrease in resolution.

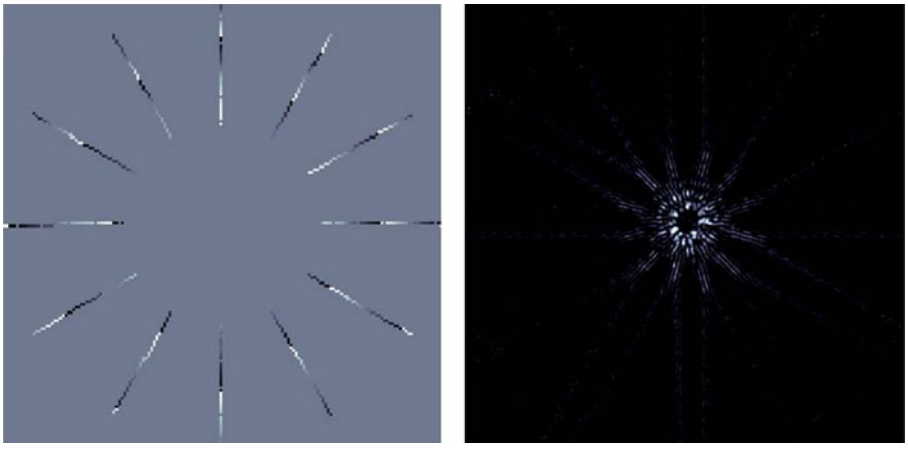

Fig. 10 Phase plot in the pupil plane (*left*) and reconstruction (*right*) of metallic ring using a 12-arm configuration

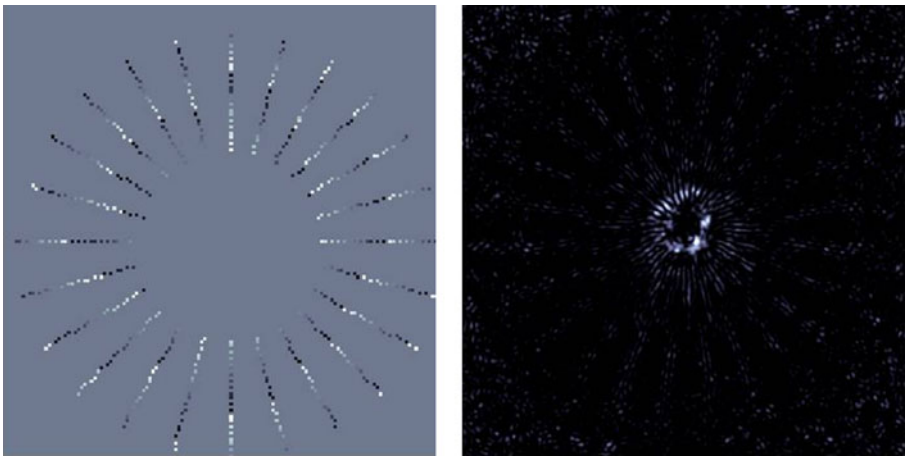

Fig. 11 Phase plot in the pupil plane (*left*) and reconstruction (*right*) of metallic ring using a 24-arm configuration

Two effects are visible in Fig. 11. First, the ringing on the target decreases as a consequence of sampling across more angular values. Second, image periodicity becomes noticable because of the larger separation between consecutive points. The zero padding was 200 and 150, in the positive and negative x- and y-directions.

The phase plot in the pupil plane and the reconstruction of the last set of experiments are shown in Fig. 12. The phase map was obtained making a full scan with constant separation along the x- and y-directions. The separation was chosen to be 2 λ. Again, the relatively large number of sampled points allows for an increase in spacing reducing the collection time to approximately 10 min, down from an expected 12 to 14 min. The outer diameter was 260 mm and the inner diameter, the section not sampled, was 105 mm. The more complete sampling of the pupil plane allows distinguishing the concentric circles of constant phase (left plot). The reconstruction does not show the ringing visible in previous figures, as there is no radial symmetry in the sampling. The Fourier spectrum matrix was padded with 250 zeros in the positive and negative x- and y- directions.

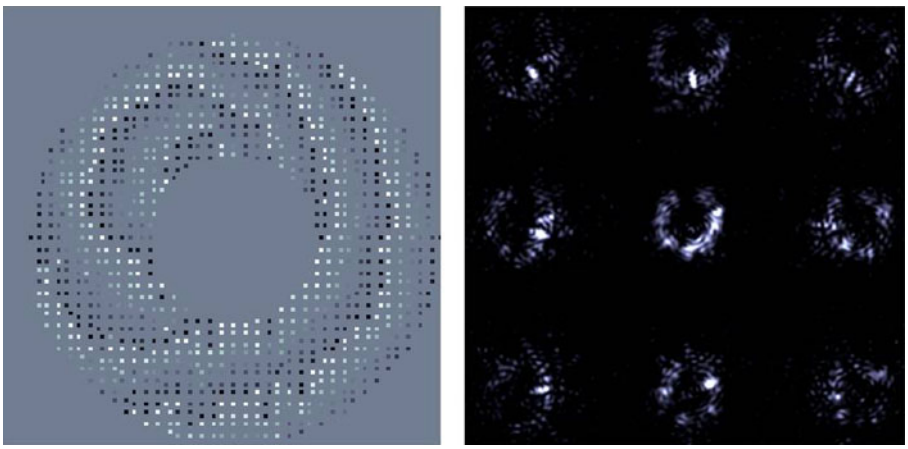

Fig. 12 Phase plot in the pupil plane (*left*) and reconstruction (*right*) of metallic ring using a full scan

The image periodicity is seen in the form of a square grid, similar to the square grid scanning pattern. The central image presents a clearer focus than the duplicates, which is a consequence of the phase correction applied to the field measurements.

The observed resolution of the reconstructed images is consistent with what is expected of an imager with the same dimensions (~260 mm) and wavelength (~3.2 mm). The image quality depends on the number of sampled points, which determines how many baselines are used for image reconstruction; therefore, more points imply a higher resolution image. The data point sets were chosen based on acquisition time and not based on the shape of the object to be detected.

3.6 Through-focus performance

In this section, we explore the system's ability to image concealed objects. A hand saw placed inside a cardboard envelope, similar to those used for mailing was scanned and imaged. The object was placed 500 mm from the test bed. The maximum separation between scanned points was 100 λ (~320 mm), and the points were made to fall on a square grid with a separation of 2 λ. Figure 13 shows the images obtained while applying the focusing algorithm to a single field scan. The focus is moved from 0 mm, in 100 mm steps, up to what was considered the clearest image. We found the empirical focus distance to be at 460 mm, and then defocused in 100 mm steps from 600 mm to 900 mm.

Although the system is capable of measuring using apertures up to 900 mm, the maximum extension used in the presented example was 320 mm. Larger apertures were not used to avoid placing the targets in the nulls of the antennas. These larger apertures can be used for targets located at greater distances. The reconstructions shown in sections 3.5 and 3.6 show the ability of the system to generate imagery, but rely on the use of simple, oversampled configurations. The next section studies the effects of redundancy on the point spread function.

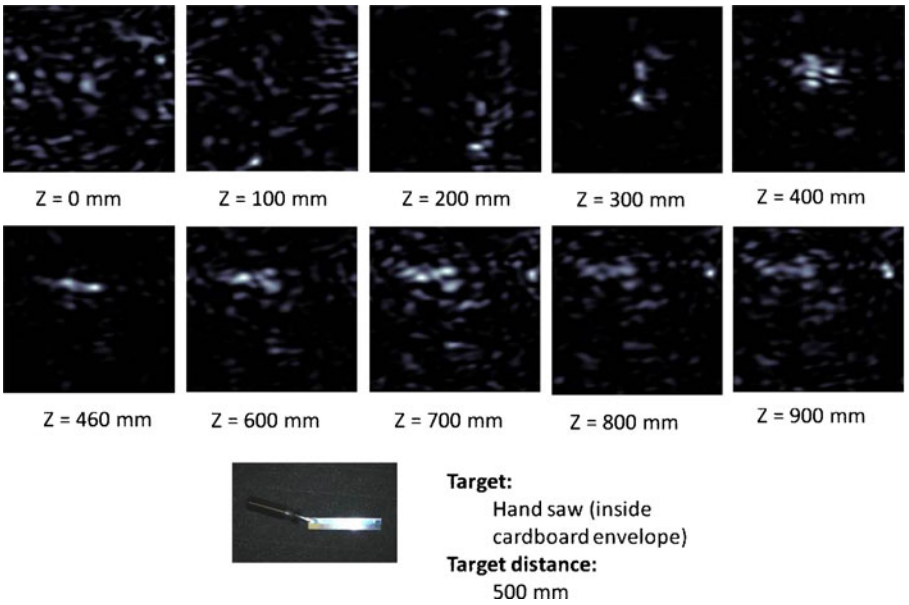

Fig. 13 Image of a hand saw inside cardboard envelope. The images were obtained by digitally focusing between 0 mm and 900 mm. The empirical focus was found to be 460 mm

4 Studies on minimally redundant aperture configurations

If two or more apertures share the same baseline along the same direction, then the same vector spatial frequency will be sampled. Although redundant sampling is not a completely negative situation, as it does not diminish image quality by itself, minimally-redundant configurations are preferred as they provide the same image quality of larger arrays with the fewest components.

The spatial frequencies sampled by a sparse or diluted array are directly linked to its shape; therefore, when choosing a configuration, the design needs to consider what frequencies are to be sampled. The baselines are vectorial quantities, meaning that the sampled frequency depends not only on the absolute separation of the detectors, but also on their orientation. The pattern of sampled spatial frequencies, also called the (u,v) plane, is dictated by the autocorrelation of the array distribution and, therefore, it impacts the modulation transfer function (MTF). The modulation transfer function (MTF) of a system is the modulus of the autocorrelation of the sampling array. However, the autocorrelation is not an invertible function and, as such, an array that yields a desired MTF cannot be calculated analytically. Numerical optimizations can be used to calculate the arrays, but are computationally expensive [14].

Two-dimensional arrays having compact, non-redundant autocorrelations were introduced by Golay in 1971 [15]. Golay arrived at these configurations using algorithms based on random guessing and by limiting those solutions to various grid patterns [14]. These configurations can be applied to arrays that have different fill factors and have been applied to imaging systems having individual apertures of varying sizes [16]. Cornwell developed algorithms with non-redundant autocorrelations, but his arrays had the limitation that the detectors need to lay on a circle. In that study, the Golay-9 array was preferred for its compactness and homogeneous distribution of its autocorrelation.

In our study, four different array configurations were compared in their ability to image a point source. Circular, cross, star, and Golay-9 distributions are used to generate scanning maps all consisting of 9 points. To emulate a nine-element array with a single detector, scans were taken in time multiplex. Figure 14 shows the chosen detector distributions and their autocorrelations. The column labeled “auto-correlation amplitude” is the side view of the autocorrelation. The maximum is the amplitude of the center lobe and side lobes with equal magnitude represent points equally sampled. The coordinates of the four maps are given in Table 2 and are normalized to fit a square of side equal to 1, expanding from -0.5 to 0.5.

The Golay configuration consists of three sets of points with the points in each set equidistant to the center and it shows a very compact and nonredundant autocorrelation. The amplitude of its side lobes show that all get correlated only once. Only twelve points are not adjacent to the center hexagon. Although the maximum number of baselines available for an array with n detectors is equal to $n(n-1)/2$, twice as many points can be obtained because of the hermitian nature of the spatial frequency plane [17]. Therefore, the maximum number of points from a 9 element array is 72, which is shown in the autocorrelation map of the Golay-9 array.

The star configuration was selected for its relatively low redundancy, as its autocorrelation is only 6 points smaller than that of the Golay-9. The autocorrelation map is not as compact as the Golay-9, but has the advantage of a simpler design. The circular array is also another type of nonredundant configuration and with a simple design. However, it lacks the compactness of the Golay distributions. The chosen circular array has constant angular separation between all detectors making it different to the arrangement

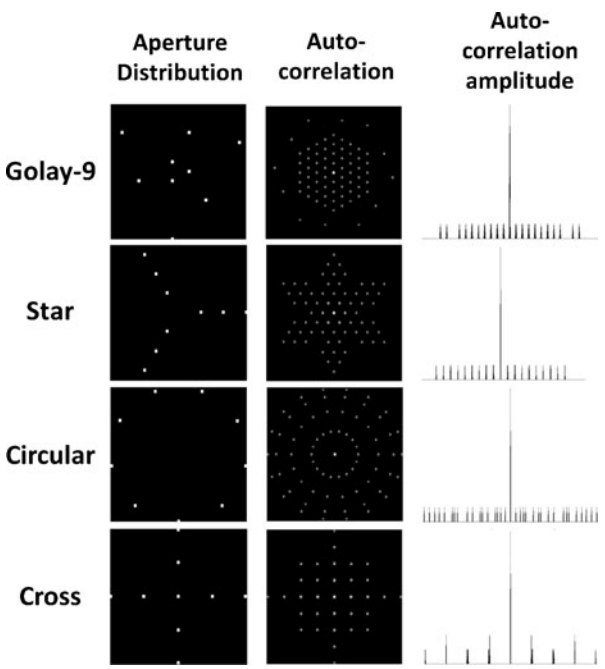

Fig. 14 Aperture arrays and their autocorrelations. The "auto-correlation amplitude" column is a side view of the cross-correlation plot

obtained with Cornwell's algorithm. Finally, the last distribution studied is the cross configuration, which is the most redundant one. The disadvantage of its redundancy is partially compensated by the simplicity of its scan format. The autocorrelation presents a uniform pattern and the spatial frequencies are harmonics of the fundamental frequency dictated by the separation of two consecutive detectors.

4.1 Analysis and assessment

The setup for these experiments was shown in Fig. 3. Because the illuminating source of the test bed is located at its center, the detectors are not able to sample an inner area 45 mm

Table 2 Normalized coordinates of the scanning maps.

Golay	(-0.07143,0.04124)	(0.07143,0.04124)	(0,0.08248)
	(0.5,-0.04124)	(0.21428,0.20620)	(-0.21428,0.4536)
	(-0.2857,0.08248)	(-0.2857,-0.4124)	(0.07143,-0.2887)
Star	(0,0.4950)	(0.0.3293)	(0,0.1637)
	(-0.1417,-0.08184)	(-0.2834,-0.1637)	(-0.4251,-0.2455)
	(0.1417,-0.0818)	(0.2834,-0.1636)	(0.4251,-0.2455)
Circular	(0.5,0)	(0.3830,0.3214)	(0.0868,0.4924)
	(-0.25,0.4330)	(-0.4698,0.1710)	(-0.4698,-0.1710)
	(-0.25,-0.4330)	(0.0868,-0.4924)	(0.3830,-0.3214)
Cross	(-0.4880,0.004)	(-0.248,0.004)	(0.004,0.004)
	(0.252,0.004)	(0.492,0.004)	(0.004,-0.4888)
	(0.004,-0.248)	(0.004,0.252),	(0.004,0.492)

in radius. For this reason, the test maps were displaced 45 mm in the positive direction of the x-axis, with respect to the center of the test bed. The dimensions for the measurements were selected so each array could be circumscribed by a circle 19.4 mm in diameter. This value was selected based on the minimum separation between any two elements in the Golay-9 array, which was chosen to be 1/2 wavelengths.

The calculated values were obtained by computing the complex fields generated by a spherical point source, with radiation propagating in free space, and measured at the detectors locations. The reconstruction was obtained by performing the inverse Fourier transform of the autocorrelation of the signals. The resulting image obtained with Fourier reconstruction was squared to better help distinguish the main lobe against the side lobes. The focusing algorithm was used for phase correction and makes the source appear to be located in the far field.

The reconstruction of the point source for the theoretical and measured values is shown in Fig. 15. The column on the right is the normalized cross-section of the slice with the maximum value and is included for comparison. The periodicity observed in the images is a result of sub-sampling and is a common artifact seen in Fourier inversion reconstructions.

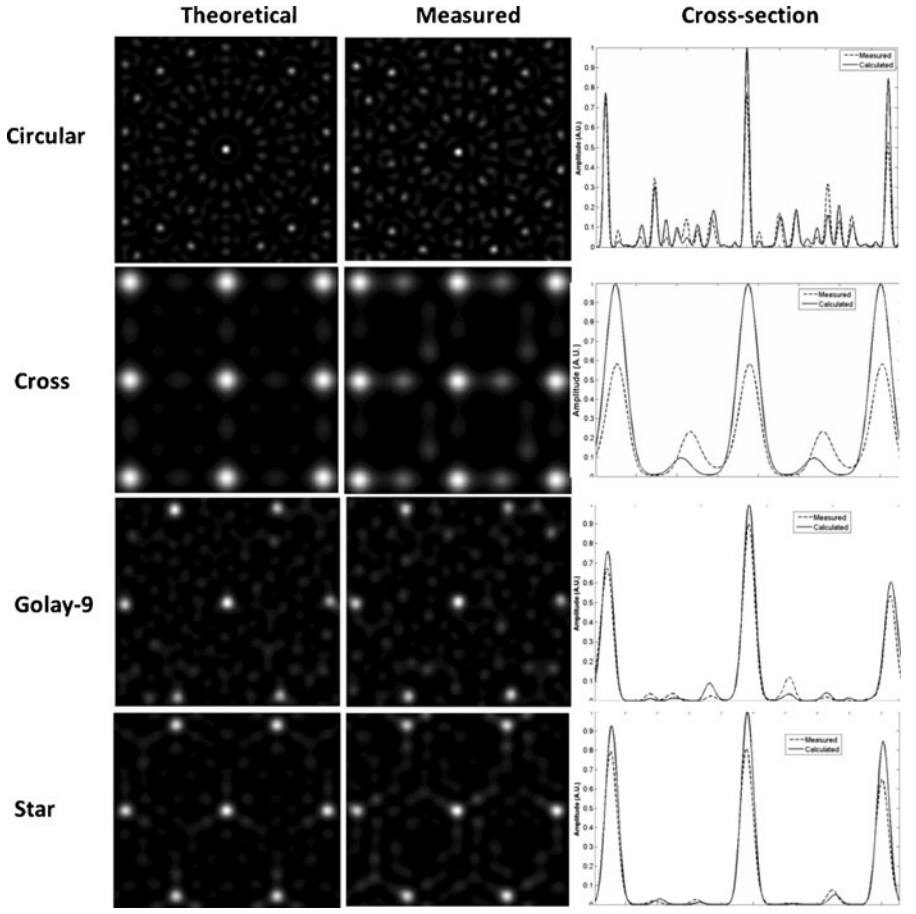

Fig. 15 Theoretical and measured values of point source reconstruction. A cross-section of the slice with the maximum value for both the theoretical and measured values is also shown

Only the largest peak and the first repetition to the left and to the right are plotted. The Fourier reconstructions were smoothed by padding the array with 200 zeros in the positive and negative x and y directions.

Figure 15 shows the calculated and measured reconstruction of a point source using 9-element circular, cross, Golay, and star configurations. For the circular configuration, a narrow center lobe can be obtained, a consequence of sampling high frequency points. However, many points are still missing from the complete spatial frequency plane and, therefore, a large amount of energy is contained in the sidelobes. The cross-section plot shows that the calculated and measured values are in good agreement. The ratio of the squared amplitudes of the measured and the calculated values is approximately 0.77, or, what is equivalent, 87.7% of the linear amplitude. The PISLR for the 9-element circular array is -14.8 dB and -16.14 dB for the calculated and measured values, respectively.

The cross pattern generates a wide center lobe, a product of the lack of sampling of high frequencies. On the other hand, the compactness of the frequency sampling means that the number of side lobes is small, although they contain a significant amount of the collected energy. The ratio of the squared amplitudes of the measured and calculated plots, as shown in the cross-section plot, is approximately 0.6, therefore, the linear ratio is approximately 77%. The computed PISLRs are -3.6 dB and -5.7 dB, for the calculated and measured values, respectively.

Calculated and measured reconstructions of a point source using the Golay-9 configuration present a slightly wider center lobe, compared to the circular distribution, but have the advantage of having very small side lobes. Also, the side lobe pattern is irregular, making it easier to distinguish the signal from the noise. The Golay-9 provides the most accurate reconstruction of the four shown in this study. A qualitative analysis of the cross-sections highlights the excellent agreement between the measured and calculated values. The ratio of the squared amplitudes is approximately 0.9, equivalent to 95% of the linear amplitudes. The computed PISLRs are -9.27 dB and -9.46 dB, for the calculated and measured values, in that order.

The reconstructions obtained using the 9-element star configuration are similar to those obtained with the Golay-9 array, but with larger side lobes. Just as the case for the circular configuration, these larger sidelobes are the effect of missing frequency components in the (u,v) plane. The ratio of the measured and calculated values is approximately 0.8, or 89% of the linear amplitudes. The computed PISLRs are -8.64 dB and -8.83 dB for the calculated and measured values, correspondingly.

5 Discussion

This study shows that a combination of aperture synthesis techniques and digital correlation can be successfully used for millimeter-wave imaging. The image resolution in all cases is consistent with what we could expect from a monolithic aperture, although obtained with a simplified array of detectors. The approach can also benefit from the used of miniaturized millimeter-wave elements mounted on integrated circuits, as opposed to using commercial off-the-shelf components. This could potentially evolve into a next generation of man-portable devices capable of imaging through barriers. Fully digital phase detection and focusing also help the development of potentially portable devices, as there is no need of physical correlators or any other phase correcting elements.

Another important feature that can be achieved using this configurable test bed is the ability to generate any desired scanning pattern. As highlighted in the studies of

configuration redundancy, the spatial frequency content of the images can be adjusted so as to sample exactly any desired frequency. This means that a full scan is not needed every time, and optimized scan patterns can be used for specific targets or situations.

6 Conclusions

We demonstrated a test bed capable of synthesizing an aperture using active mmW illumination and digital correlation. The potential applications for this technology include seeing through barriers and detection and identification of concealed objects. The complex electric field, scattered from a physical target, was measured across the pupil plane by a configurable array of detectors. Using several array configurations, imaging of objects standing at distances between 430 mm and 660 mm was obtained. The detected mmW signals were down-converted using a heterodyne receiver from 94 GHz to 20 MHz. Down-converted signals were sampled by a high speed digitizer for storage and offline processing. A custom made algorithm for phase detection was successfully applied. Digital phase detection was achieved by replicating conventional quadrature demodulators substituting analog component by digital operations. The complex fields were stored in a two-dimensional complex matrix, in positions analogous to the sampled location. A digital focusing algorithm was applied at this point to virtually locate the source in the far field, therefore allowing the use of conventional reconstruction methods. This focusing algorithm could potentially be used for three-dimensional imaging. Finally, in the image formation process, the sampled pupil plane was autocorrelated and Fourier inversion was applied. Images obtained using the described algorithm show the progression in image quality as the sampling pattern complexity increases. Image quality was found to be consistent with the theoretical resolution for an imaging system of the given wavelength and aperture dimensions.

A study on the point spread function of four common detector configurations was performed. The redundancy of the autocorrelation of these configurations was shown to have an effect on the point spread function, specifically on the ratio between the mainlobe and the sidelobes. The agreement between measured and expected values also show the flexibility provided by the system to create the desired configuration through a programmable user interface.

Acknowledgments This work was supported by Northrop Grumman Corporation Aerospace Systems, Melbourne, Florida.

References

1. T.W. Du Bosq, J.M. Lopez-Alonso, and G.D. Boreman, "Millimeter wave imaging system for land mine detection," Applied Optics. **45**, 22, p. 5686-5692 (2006)
2. C. Hua-Mei, L. Seungsin, R.M. Rao, M.A. Slamani, and P.K. Varshney, "Imaging for concealed weapon detection: a tutorial overview of development in imaging sensors and processing," Signal Processing Magazine, IEEE. **22**, 2, p. 52-61 (2005)
3. S. Oka, H. Togo, N. Kukutsu, and T. Nagatsuma, "Latest trends in Millimeter-Wave Imaging Technology," Progress in Electromagnetics Research Letters. **1**, p. 197-204 (2008)
4. L. Yujiri, M. Shoucri, and P. Moffa, "Passive millimeter wave imaging," Microwave Magazine, IEEE. **4**, 3, p. 39-50 (2003)
5. A. Thompson, J. Moran, and G. Swenson, *Interferometry and Synthesis in Radio Astronomy*, (John Wiley & Sons, 2001)

6. A.R. Harvey, and R. Appleby, "Passive mm-wave imaging from UAVs using aperture synthesis," The Aeronautical Journal. **107**, 87, (2003)
7. Y. Xue, J. Miao, G. Wan, A. Hu, and F. Zhao. *Development of the Disk Antenna Array Aperture Synthesis Millimeter Wave Radiometer*. in *Millimeter Waves, 2008. GSMM 2008. Global Symposium on*. 2008. (2008)
8. L. Qingxia, C. Ke, G. Wei, L. Liang, H. Fangmin, and C. Liangbing. *An aperture synthesis radiometer at millimeter wave band*. in *Microwave and Millimeter Wave Technology, 2008. ICMMT 2008. International Conference on*. 2008. (2008)
9. L. Zhang, Y. Hao, C.G. Parini, and J. Dupuy. *An experimental millimetre wave imaging system*. in *Antennas and Propagation Conference, 2008. LAPC 2008. Loughborough*. 2008. (2008)
10. S.S. Ahmed, A. Schiess, and L.P. Schmidt. *Near field mm-wave imaging with multistatic sparse 2D-arrays*. in *Radar Conference, 2009. EuRAD. European*. 2009. (2009)
11. D.M. Sheen, D.L. McMakin, and T. Hall, "Near-field three-dimensional radar imaging techniques and applications," Applied Optics. **49**, 19, p. E83-E93 (2010)
12. J.M. Blackledge, *Quantitative Coherent Imaging*, (Academic Press Inc, San Diego, 1989)
13. C.A. Balanis, *Antenna theory : analysis and design*. 2nd ed, (Wiley, New York, 1997)
14. N.J. Miller, M.P. Dierking, and B.D. Duncan, "Optical sparse aperture imaging," Applied Optics. **46**, 23, p. 5933-5943 (2007)
15. M.J.E. Golay, "Point Arrays Having Compact, Nonredundant Autocorrelations," Journal of the Optical Society of America. **61**, 2, p. 272-& (1971)
16. A.J. Stokes, B.D. Duncan, and M.P. Dierking, "Improving mid-frequency contrast in sparse aperture optical imaging systems based upon the Golay-9 array," Optics Express. **18**, 5, p. 4417-4427 (2010)
17. M. Peichl, H. Suess, M. Suess, and S. Kern, "Microwave imaging of the brightness temperature distribution of extended areas in the near and far field using two-dimensional aperture synthesis with high spatial resolution," Radio Science. **33**, 3, p. 781-801 (1998)